WILEY-VCH

3D Mapping of Crystallographic Phase Distribution using Energy-Selective Neutron Tomography

Robin Woracek, Dayakar Penumadu*, Nikolay Kardjilov, Andre Hilger, Mirko Boin, John Banhart, Ingo Manke

Mr. R. Woracek, Prof. D. Penumadu
College of Engineering, The University of Tennessee, 223 Perkins Hall, Knoxville, TN, 37996, USA
E-mail: dpenumad@utk.edu
Dr. N. Kardjilov, Dr. A. Hilger, Dr. M. Boin, Prof. J. Banhart, Dr. I. Manke
Institute of Applied Materials, Helmholtz-Zentrum Berlin, Hahn-Meitner-Platz 1, 14109 Berlin, Germany

Recently demonstrated diffraction-based imaging using X-rays and transmitted electrons offers exciting prospects for non-destructive three-dimensional (3D) microstructural characterization of crystalline materials.[1-6]. However, because of the limited penetration power of X-rays and electrons into structural alloys, neutrons are required for bulk investigations,[1] which are crucial to understand the meso-scale effects for polycrystalline materials.[2] Here we introduce a tomography method for non-destructive 3D mapping of crystallographic phases that overcomes critical limitations of existing methods by providing spatially resolved phase fractions within the bulk (centimeter range) of samples with micrometer-scale resolution. We demonstrate spatial mapping of two phases in (metastable 304L stainless) steel samples that exhibit strain-induced martensitic phase transformation after being subjected to tensile and torsional deformation. The technique leverages diffraction contrast due to Bragg scattering and the large penetration power of neutrons through high-atomic-number-element-based structural materials, offering a wide range of potential applications for characterization of natural and advanced materials.

Studying crystallographic phase distributions and phase transformations is important, as these microstructural properties largely govern the global mechanical properties of these materials. Understanding the relation between dislocation density evolution and phase transformations is essential for developing the theoretical framework in computational materials science, especially as it relates to the Materials Genome Initiative. There has been extensive research of phase-transformed materials, e.g., shape-memory alloys,[3] recrystallization processes,[4] and materials exhibiting the transformation induced plasticity (TRIP) effect.[5] "Further understanding of the transformation mechanisms depends critically on the available characterization techniques," which is "crucial for the development of fundamental phase transformation models and to develop steels with superior properties."[5] Existing techniques (e.g., electron backscatter diffraction, electron microscopy, X-ray and synchrotron diffraction, optical microscopy, magnetic and ultrasonic measurements) are destructive and/or limited to the surface or to small-sized specimens. Diffraction contrast tomography[6] and 3D-XRD,[7] as employed at synchrotron sources, use the diffraction signal of individual grains to produce 3D maps of grain shape and crystallographic orientation and are, in principle, capable of non-destructive phase mapping. However, those techniques are usually constrained to small sample sizes consisting of a limited number of grains with a high degree of mosaicity, which is not the case for plastically deformed materials. Our energy-selective neutron tomography approach provides a non-destructive 3D representation of phase fractions in large-specimen volumes (cm^3 range). The achievable spatial resolution (approximately $20\times20\times20$ µm^3 voxel volume) and sensitivity for quantifying phase fractions, which also is determined by the grain size, is at least three orders of magnitude more precise than what is possible with neutron diffraction instruments (> $500\times500\times500$ µm^3).

Using neutrons of particular wavelengths (energy), it is possible to probe the energy dependence of the sample's attenuation coefficient. The elastic coherent scattering cross

section changes suddenly at well-defined wavelengths λ, defined by Bragg's law

($\lambda = 2d_{hkl}\sin\theta^B$; d_{hkl}: lattice spacing, θ^B: Bragg angle). In monochromatic transmission

measurements, the "missing" portion of the neutron beam is observed while neutrons are

scattered at certain angles θ^B (typically detected in a diffraction instrument). If the wavelength

is increased to larger than $\lambda = 2d_{hkl}\sin90° = 2d_{hkl}$, Bragg scattering for the corresponding

lattice planes *hkl* cannot occur, and the transmitted intensity increases suddenly,

corresponding to a well-defined Bragg edge (see **Figure 1** and Supplementary **Figure S1** for

austenite and α-martensite phases of iron[8]). This methodology has been used to produce 2D

strain[9-11] and texture[12, 13] maps. The transmission method has also been used to determine

crystallographic phase fractions, but without spatial resolution.[9, 14-17]

To demonstrate the transmission technique for 3D phase mapping, we studied metastable

stainless steel (ASTM standard 304L) exhibiting the TRIP effect, where austenite (having a

face-centered cubic structure, fcc) transforms to martensite (consisting of body-centered

cubic, bcc, and hexagonal closest packed, hcp, structures), when subjected beyond a certain

plastic strain.[18] For this class of materials, there is a significant amount of literature

regarding uniaxial deformation,[19, 20] and recently, more complex loading in torsional shear

has been investigated.[21, 22] A previous study indicates that the degree of elastic anisotropy

varies depending on whether a sample is loaded in pure torsion or pure tension.[23] Any plastic

deformation is prone to inhomogeneity that, due to anisotropy, can result in distinct failure

mechanisms; therefore, the comparison of loading paths is of significant interest.

Five samples were investigated (see radiographs in Figure 1; detailed dimensions in

Supplementary **Figure S2**). Two samples were deformed in pure tension to a theoretical

engineering strain of 108% ("TEN-med"; 5.4 mm axial deformation) and 144% ("TEN-max";

7.2 mm axial deformation). Two samples were deformed in pure torsion to a maximum shear

stress of 100% ("TOR-med"; 71.5° twist) and 250% ("TOR-max"; 179° twist). The non-

deformed sample ("VIR") was used as a reference corresponding to no external mechanical stress. Additional details on samples and mechanical testing are described in the Supplementary Methods (stress vs. strain curves are shown in Supplementary **Figure S3**). We expected the regions of highest strains to exhibit the largest martensitic phase transformation, and torsion provides an elegant way of controlling the amount of phase transformation in the radial direction (Supplementary **Figure S4**).

Energy-selective neutron transmission measurements can be performed at spallation sources using the time-of-flight information and a suitable time-resolving detector or at reactor sources, if the wavelength can be chosen accordingly. For the results presented herein, we used the dedicated neutron-imaging beamline CONRAD at the reactor source at Helmholtz-Zentrum Berlin and a tunable double-crystal monochromator (details in Experimental Section).

Radiography: For initial investigation, Bragg edge spectra were obtained for all five samples simultaneously in one orientation (see Figure 1a). The Bragg edge spectra were normalized by the open beam (no sample) spectrum, and the resulting spectra for a region of interest (ROI) are shown in Figure 1b.

Tomography: Tomographic scans were performed by recording 180 projections over a 360° range before (4.1 Å) and after (4.3 Å) the 'Bragg cut-off' corresponding to the austenitic phase. The 'Bragg cut-off' for the martensitic phase is slightly shifted towards smaller wavelengths compared to the austenitic phase, resulting in attenuation differences between the two phases in the data taken at 4.1 Å. We used filtered back-projection algorithms for parallel beam reconstruction to individually reconstruct the tomographic data sets for each wavelength. **Figure 2a** shows a cut through the middle of the 3D-reconstructed volume data (center of the samples) taken 4.3 Å. The attenuation coefficient is uniform throughout the samples and unaffected by differences in the elastic coherent scattering cross section. In contrast, the reconstructed volume of the measurement at 4.1 Å (Figure 2b) shows distinct differences in

the reconstructed attenuation coefficient. The transmitted intensity is higher for regions with larger martensitic phase content due to the different Bragg edge position. The reconstructed data taken at 4.1 Å already provides the 3D crystallographic phase distribution of austenite and martensite. However, for optimal quantification and to exclude any possible influence of slight material or signal inhomogeneities, the reconstructed slices belonging to 4.1 Å were individually normalized by the reconstructed slices belonging to 4.3 Å (Figure 2c-e). In this case, if mostly austenite is present, the resulting voxel value will be small (e.g., the pure austenitic phase in the virgin sample has a gray value of ~0.7, indicated as blue in Figure 2c-e) while the values will be closer to 1 if primarily martensite is present (i.e., pure martensitic phase in center of the maximum tensile sample has a gray value of 0.97, indicated as red). An assigned linear weighting factor corresponds to a known weight fraction for each voxel of the reconstructed volume.

Line profiles, presented in **Figure 3**, show the phase distribution across the diameter of the torsion samples and along the height of the tensile samples. There is good agreement when the phase fraction values are compared to previously published data[21] (see Supporting Information) that describe torsion samples of the same material (304L) investigated by synchrotron diffraction, using small specimen extracted from the deformed samples. Figure 3 includes derived phase fractions from complementary neutron diffraction measurements performed at the E3 instrument at HZB (see Experimental Section), and the results for the tensile samples are in good agreement with the information derived from the tomography data. For the torsion samples, the diffraction results show a trend identical to the tomography data; however, sharp gradients could not be captured because of the relatively large gauge volume used in neutron diffraction. For sample "TOR-max", the theoretical α-martensite phase evolution is shown using the Olson–Cohen model[24] and parameters described in[21] (see Supporting Information) with good agreement between the model and experiment.

5

This study presents a new non-destructive characterization method that allows the spatial distribution and volumetric extent of crystallographic phases within the bulk of large sample volumes to be determined *with superior spatial resolution*. It has the invaluable advantage of being able to reveal inhomogeneities within the measured volume, which otherwise may remain undetected. The tomographic reconstruction allows the visualization of geometric differences such as cracks and holes simultaneously with the crystallographic phase identification. The technique opens up new paths for investigations of materials in various fields of science, e.g. physical sciences, materials research, geosciences and even biology or medical sciences (e.g. bone structures using ultra-cold neutrons). By investigating several Bragg edges simultaneously (either using the time-of-flight or monochromator approach), the accuracy of such measurements can be further improved, while even allowing more than two phases to be mapped.

Experimental Section

Neutron Imaging Instrumentation

The energy selectivity at the cold neutron imaging beamline CONRAD at the reactor source at Helmholtz-Zentrum Berlin (HZB, Germany) was achieved by employing a tunable double-crystal monochromator consisting of one pyrolytic graphite crystal (PCG) monochromator in the upper and lower position, each with a mosaic spread of 0.8°. The wavelength band has an approximate resolution of $\Delta\lambda/\lambda = 3\%$ and can be tuned freely between 2.0 and 6.5 Å while the beam position remains unchanged[25]. The neutron detector used at HZB consisted of a Li6F scintillator screen of 200 µm thicknesses and an optical CCD camera (2048×2048 pixels) with an objective lens. The effective pixel size in the presented data was 53.6 µm, resulting in a 11×11 cm^2 field of view (FOV), which allowed all five samples to be accommodated. It should be noted that the presented neutron-imaging-based approach is capable of spatial resolutions below 20 µm[26] if the sample grains are small enough.

6

Complementary Neutron Diffraction

Complementary neutron diffraction measurements were performed at the constant wavelength diffractometer E3 at HZB ($\lambda = 1.486$Å) with the goal of verifying the transmission-based results. A primary slit of 2×2 mm^2 and a 2 mm radial collimator (oscillating) were used to define the probed volume within the sample. The tensile samples were incrementally scanned along the height over approximately 20 mm around the sample center. The torsion samples were scanned at 13 locations along the sample cross section, starting from the sample center and going 4.5 mm in both directions. In each case, three bcc reflections (110, 200, 211) and three fcc reflections (111, 200, 220) were recorded. The neutron ray tracing package McStas[27] was used to correct for the variation in detected neutron intensities due to the different neutron path lengths and partially filled gauge volumes (close to the surface) by simulating an ideal powder sample and normalizing the measured data to the simulated data. From this information, the phase fractions were determined by weighting all bcc and fcc peak intensities. The resulting plots are included in Figure 3.

Supporting Information
Supporting Information is available from the Wiley Online Library or from the author.

Received: ((will be filled in by the editorial staff))
Revised: ((will be filled in by the editorial staff))
Published online: ((will be filled in by the editorial staff))

[1]   B. C. Larson, W. Yang, G. E. Ice, J. D. Budai, J. Z. Tischler, Nature 2002, 415, 887.

[2]   H. F. Poulsen, *Three-Dimensional X-Ray Diffraction Microscopy: Mapping Polycrystals and their Dynamics*, Springer, Heidelberg 2004.

[3]   M. A. Pfeifer, G. J. Williams, I. A. Vartanyants, R. Harder, I. K. Robinson, Nature 2006, 442, 63.

[4]   A. King, G. Johnson, D. Engelberg, W. Ludwig, J. Marrow, Science 2008, 321, 382.

[5]   P. Bleuet, E. Welcomme, E. Dooryhee, J. Susini, J.-L. Hodeau, P. Walter, Nat Mater 2008, 7, 468.

[6]   H. H. Liu, S. Schmidt, H. F. Poulsen, A. Godfrey, Z. Q. Liu, J. A. Sharon, X. Huang, Science 2011, 332, 833.

[7]   J. Banhart, *Advanced tomographic methods in materials research and engineering*, Oxford University Press New York, 2008.

[8]   R. D. Doherty, D. A. Hughes, F. J. Humphreys, J. J. Jonas, D. J. Jensen, M. E. Kassner, W. E. King, T. R. McNelley, H. J. McQueen, A. D. Rollett, Materials Science and Engineering: A 1997, 238, 219.

[9]   J. Ma, I. Karaman, Science 2010, 327, 1468.

[10]   S. E. Offerman, N. H. van Dijk, J. Sietsma, S. Grigull, E. M. Lauridsen, L. Margulies, H. F. Poulsen, M. T. Rekveldt, S. van der Zwaag, Science 2002, 298, 1003.

[11]   M. Militzer, Science 2002, 298, 975.

[12]   M. Boin, Journal of Applied Crystallography 2012, 45, 603.

[13]   J. R. Santisteban, L. Edwards, M. E. Fizpatrick, A. Steuwer, P. J. Withers, Applied Physics A: Materials Science & Processing 2002, 74, s1433.

[14]   A. Steuwer, J. R. Santisteban, P. J. Withers, L. Edwards, M. E. Fitzpatrick, Journal of Applied Crystallography 2003, 36, 1159.

[15]   R. Woracek, D. Penumadu, N. Kardjilov, A. Hilger, M. Strobl, R. C. Wimpory, I. Manke, J. Banhart, Journal of Applied Physics 2011, 109, 093506.

[16]   J. R. Santisteban, L. Edwards, V. Stelmukh, Physica B: Condensed Matter 2006, 385-386, Part 1, 636.

[17]   J. R. Santisteban, M. A. Vicente-Alvarez, P. Vizcaino, A. D. Banchik, S. C. Vogel, A. S. Tremsin, J. V. Vallerga, J. B. McPhate, E. Lehmann, W. Kockelmann, Journal of Nuclear Materials 2011.

[18]   M. A. M. Bourke, J. G. Maldonado, D. Masters, K. Meggers, H. G. Priesmeyer, Materials Science and Engineering: A 1996, 221, 1.

[19]   A. Steuwer, J. R. Santisteban, P. J. Withers, L. Edwards, Physica B: Condensed Matter 2004, 350, 159.

[20]   A. Steuwer, P. J. Withers, J. R. Santisteban, L. Edwards, Journal of Applied Physics 2005, 97, 074903.

[21]   J. Huang, S. C. Vogel, W. J. Poole, M. Militzer, P. Jacques, Acta Materialia 2007, 55, 2683.

[22]   M. Bayerlein, H. J. Christ, H. Mughrabi, Materials Science and Engineering: A 1989, 114, L11.

[23]   J. A. Venables, Philosophical Magazine 1962, 7, 35.

[24]   Y. Tomota, H. Tokuda, Y. Adachi, M. Wakita, N. Minakawa, A. Moriai, Y. Morii, Acta Materialia 2004, 52, 5737.

[25]   E. Cakmak, H. Choo, K. An, Y. Ren, Materials Letters 2011, 65, 3013.

[26]   E. Cakmak, H. Choo, K. An, Y. Ren, Acta Materialia 2012, 60, 6703.

[27]   R. Woracek, J. R. Bunn, D. Penumadu, C. R. Hubbard, Applied Physics Letters 2012, 100, 191904.

[28]   G. B. Olson, M. Cohen, MTA 1975, 6, 791.

[29]   W. Treimer, M. Strobl, N. Kardjilov, A. Hilger, I. Manke, Applied Physics Letters 2006, 89, 203504.

[30] S. H. Williams, A. Hilger, N. Kardjilov, I. Manke, M. Strobl, P. A. Douissard, T. Martin, H. Riesemeier, J. Banhart, Journal of Instrumentation 2012, 7, P02014.

[31] K. Lefmann, K. Nielsen, Neutron News 1999, 10, 20.
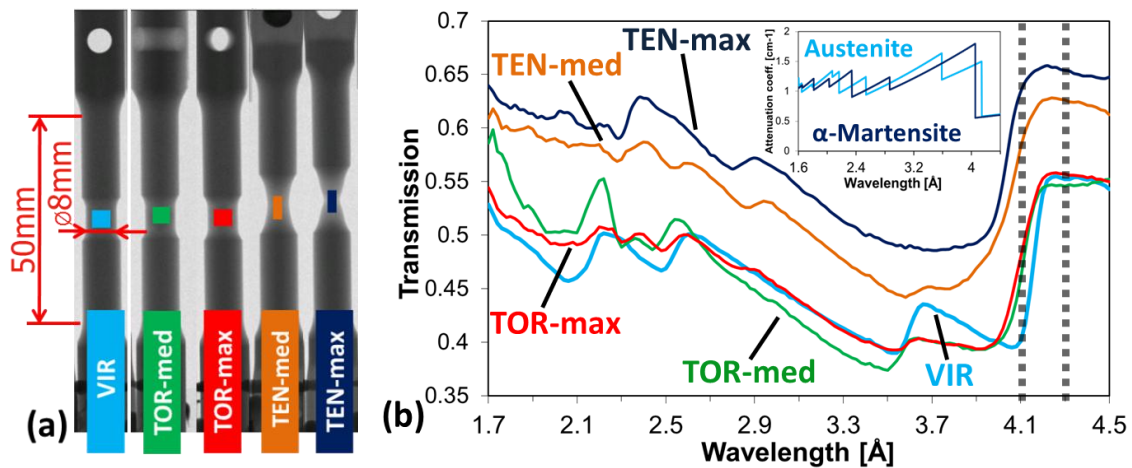
Figure 1. Transmission image and transmission spectra: a) Radiograph of samples with region of interest (ROI) depicted, which was used for the plot in Figure 1b. b) Bragg edge transmission spectra (131 mono-energetic radiographic projections between 1.7 Å and 4.5 Å with an exposure time of 240 seconds/projection) for the center gauge area of the five samples. The non-deformed sample "VIR" is purely austenitic, and only Bragg edges corresponding to austenite are visible. The center of tensile sample "TEN-max" is fully transformed to martensite (compare to theoretical attenuation coefficients depicted in inset and Figure S1) while "TEN-med" is only partially transformed over the selected ROI. The two torsion samples show Bragg edges of both crystallographic phases in the gauge area, which is anticipated, as the center of the sample is not expected to transform to martensite since the applied shear stress there is zero; hence tomographic reconstruction is needed for further quantification. Investigating regions outside the gauge area, the Bragg edge spectra are identical to those of the virgin sample, proving that no (significant) deformation occurred. The dotted vertical lines indicate the wavelengths where tomographic scans were performed.

10
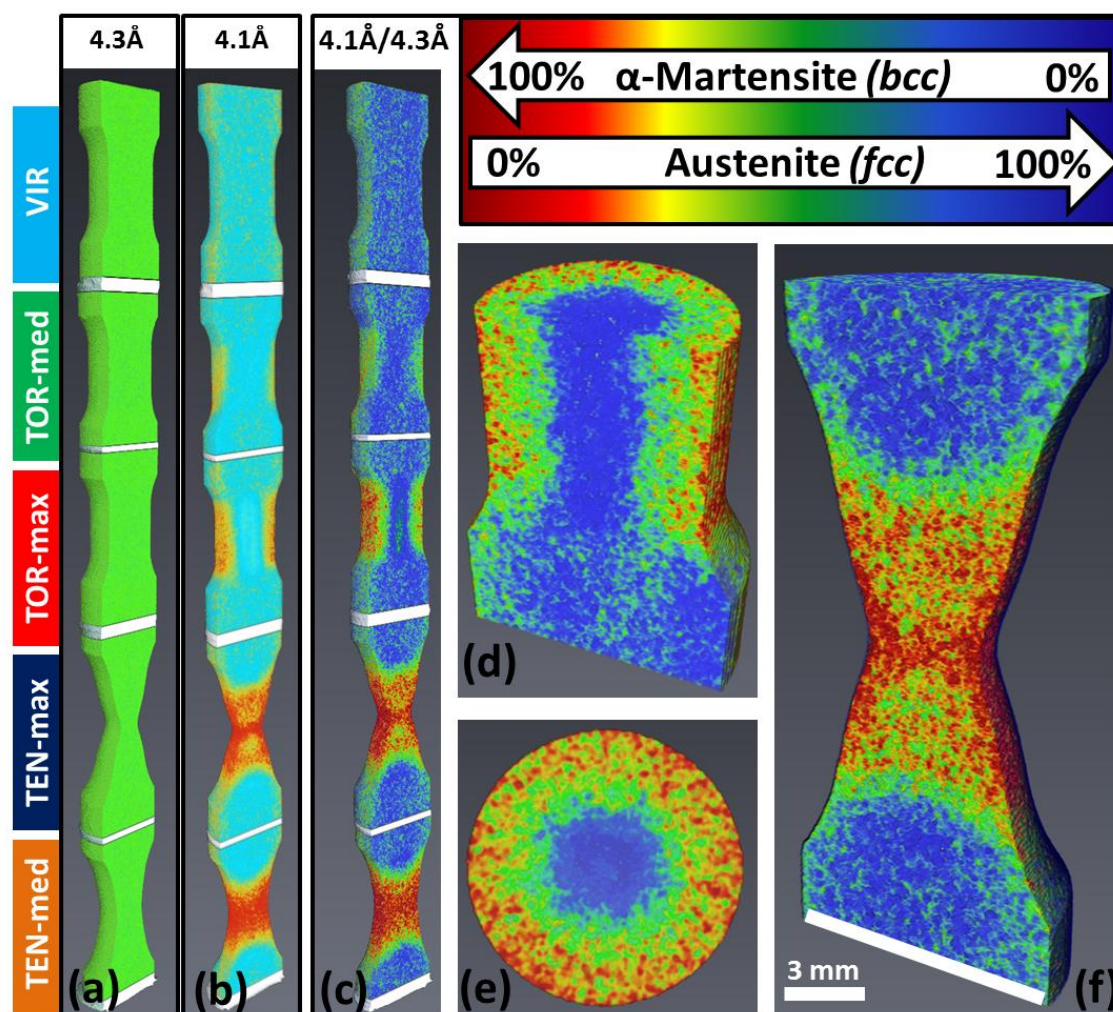
Figure 2. Tomographic reconstructions: a,b) Center slice of the tomographic reconstruction of the five samples (samples were cut to a region around the gauge area and glued atop one another to be measured simultaneously) for wavelengths before (4.1 Å) and after (4.3 Å) the 'Bragg cut-off' of austenite. c-f) The reconstructed data sets were divided to accentuate the transmission intensities due to Bragg diffraction (4.1 Å/4.3 Å), and phase fractions were assigned. d,e) The radial dependence of the phase transformation in the torsion sample "TOR-max" is clearly visible in the tomographic reconstruction when viewing the cross section. f) Close-up of the tensile sample "TEN-max" showing that the necking region and regions close to the gauge area surface have the highest martensitic phase contents.
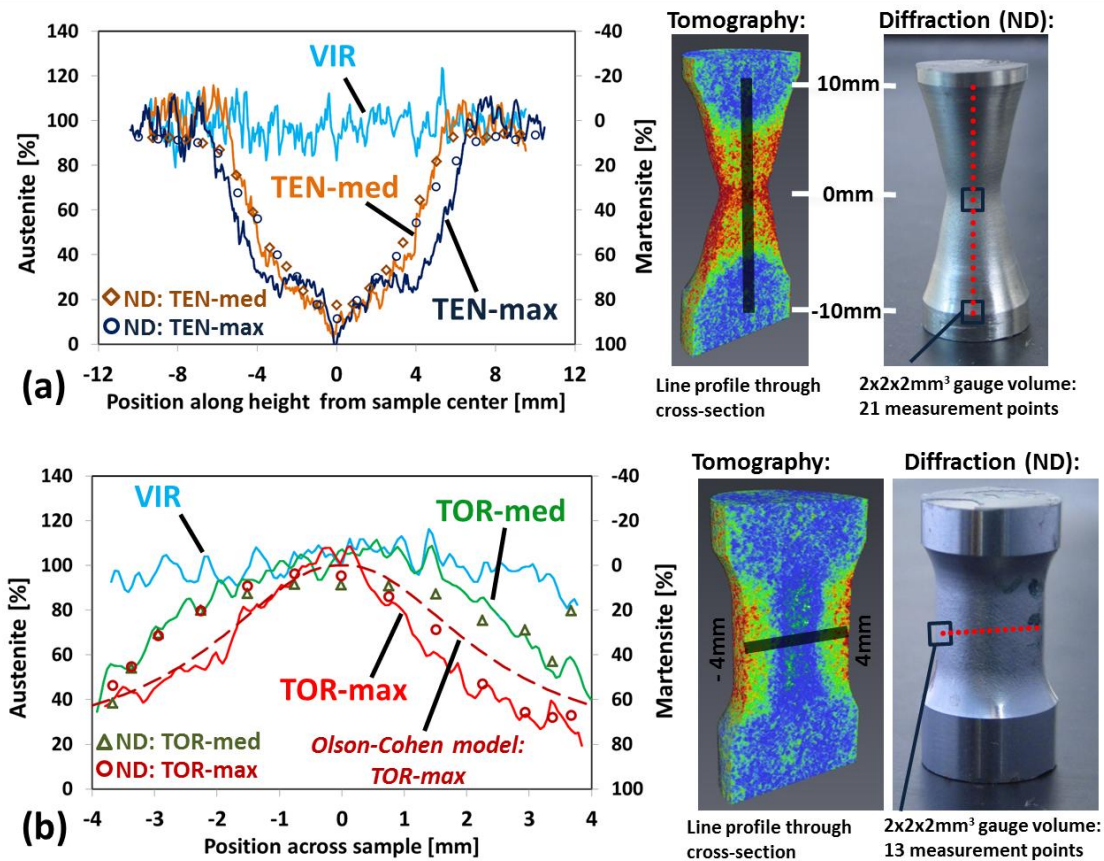
Figure 3. Line profiles along and across the reconstructed tomographic data showing the austenitic and martensitic phase fractions. Neutron-diffraction-based results (labeled "ND") are also included to refer to a standardized characterization method. The diffraction results were obtained using a $2\times2\times2$ mm^3 gauge volume and by scanning along/across the samples. a) Phase fractions along the height of the tensile samples and the virgin sample. Both samples subjected to tensile loading were fully transformed to martensite in the necking region. b) Phase fractions across the center of the torsion samples and the virgin sample. For the torsion samples, the maximum phase changes occurred in the region near the outer diameter as expected, and no transformation occurred in the sample center. For "TOR-max", the theoretical α-martensite phase evolution is predicted using the Olson–Cohen model[21, 24].

The table of contents entry:

This paper introduces nondestructive three-dimensional mapping of crystallographic phases providing distribution of phase fractions within the bulk (centimeter range) of samples with micrometer-scale resolution. The novel neutron tomography based technique overcomes critical limitations of existing techniques and offers a wide range of potential applications. It is demonstrated for steel samples exhibiting phase transformation after being subjected to tensile and torsional deformation.

Keyword: crystallographic characterization

R. Woracek, D. Penumadu*, N. Kardjilov, A. Hilger, M. Boin, J. Banhart, I. Manke

Title: 3D Mapping of Crystallographic Phase Distribution using Energy-Selective Neutron Tomography
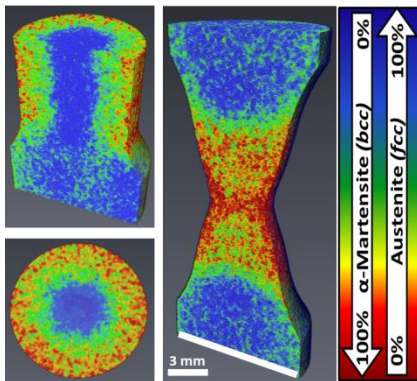
ToC figure

Supporting Information